Spectroscopic and computational insights on catalytic synergy in bimetallic aluminophosphate catalysts

Matthew E. Potter,[a,b]* A. James Paterson,[b] Bhoopesh Mishra,[c] Shelly D. Kelly,[d] Simon R. Bare,[d] Furio Corà,[e] Alan B. Levy[f] and Robert Raja[b]*

[a] Department of Chemical and Biochemical Engineering, Georgia Institute of Technology, 311 Ferst Drive, Atlanta, GA 30332, USA. E-mail: matthew.potter@chbe.gatech.edu.

[b] School of Chemistry, University of Southampton, Southampton, Hampshire, United Kingdom, SO17 1BJ. *Fax: 02380 592144; Tel: 02380 593781; E-mail: R.Raja@soton.ac.uk.

[c] Physics Department, Illinois Institute of Technology, Chicago, IL, 60016, USA.

[d] UOP LLC, A Honeywell Company, 25 East Algonquin Road, Des Plaines, IL 60017, USA.

[e] Department of Chemistry, University College London, 20 Gordon Street, London WC1H 0AJ, UK.

[f] Honeywell Int, 101 Columbia Road, Morristown, NJ 07962, USA.

Supporting Information Placeholder

ABSTRACT: A combined electronic structure computational and X-ray absorption spectroscopy study was used to investigate the nature of the active sites responsible for catalytic synergy in Co-Ti bimetallic nanoporous frameworks. Probing the nature of the molecular species at the atomic level has led to the identification of a unique Co-O-Ti bond, which serves as the loci for the superior performance of the bimetallic catalyst, when compared with its analogous monometallic counterpart. The structural and spectroscopic features associated with this active site have been characterized and contrasted, with a view to affording structure-property relationships, in the wider context of designing sustainable catalytic oxidations with porous solids.

Introduction

Growing global concerns over greenhouse gas emissions and finite energy resources have facilitated growth in many areas of materials science. Catalysis is no exception. The desire for cheaper, cleaner and more efficient technologies demands that any novel catalytic material possessing distinctive activity/selectivity characteristics be stringently investigated, aiding the understanding and promoting the judicious design of more efficient catalysts.[1-3] In order to reach this goal, detailed knowledge of the precise nature and behaviour of catalytically-active sites at the molecular level is of fundamental importance. A meticulous understanding of structure-property relationships between such sites and the surrounding matrix is also necessary before such a catalyst can be rationally designed.[4] In the vast majority of heterogeneous catalysts such tempting notions are far from trivial, owing to the difficulties in precise active-site placement, combined with the need for more advanced *in situ* techniques to specifically probe and engineer active surface sites, which may constitute only a small fraction of the whole system.[5] Single site heterogeneous catalysts (SSHCs), such as microporous zeotypic solids, where the active sites are in an uniform crystalline environment that is well-distributed throughout the material, are potentially well-suited to overcome some of the above limitations.

Recent research has witnessed widespread developments in the field of multi-metallic zeotype catalysts, with a large proportion exploiting the idea of catalytic synergy. A number of examples exist in the literature whereby the combination of two metal dopants results in a favourable modification of the catalytic profile, highlighting potential benefits for the industrial applicability of such designed materials.[6-8] While the notion is undoubtedly appealing, the inclusion of a second metal introduces a further level of complexity, that demands a more stringent control from a synthetic perspective. A more detailed knowledge of the local structural environment and associated structure-property relationships is required, not just between the host and the dopants but also between the different heteroatom substituents themselves. To quantify such interactions at the molecular level requires a detailed understanding of the nature of the active sites, and it is necessary to employ a range of physico-chemical, *operando* and spectroscopic characterisation techniques, that are best complemented when integrated with atomic level modelling studies.[9-15]

In our recent work[16] we extended the family of transition-metal doped aluminophosphate (AlPO) frameworks,[10,17,18] to obtain isomorphous incorporation of bimetallic active centres, that display superior catalytic activity in oxidation reactions (Figure S1 and Table S1).[16] Through a rational selection of appropriate metal combinations and synthetic strategy, it is possible to engineer and exploit synergic interactions between individual metal sites, deliberately placed within sufficiently close proximity such that their local geometry and electronic structure is modified to facilitate catalytic improvements. It is possible to engineer this phenomenon not only between different dopants, but also for different industrially relevant catalytic transformations.[9,16,19-21]

In this paper we discuss the synergic effects obtained by isomorphously substituting cobalt and titanium ions simultaneously into the same AlPO-5 framework, to yield a bimetallic Co-TiAlPO-5 system. We have previously shown that individually these two metal dopants (as monometallic entities) are capable of

catalysing a range of oxidation reactions.[22,23] However, we have recently demonstrated[9,16] that their simultaneous incorporation has the potential to induce catalytic synergy. Comprehensive UV/Vis studies demonstrated that the local environment around the titanium becomes more tetrahedral when cobalt is present in the same framework.[16] The bimetallic catalyst facilitates more efficient oxidant-activation, increasing product yields. We now present a comprehensive electronic-structure DFT calculations and complementary *in situ* extended X-ray absorption fine structure (EXAFS) spectroscopy study, to elucidate the nature of the active cobalt site within the bimetallic CoTiAlPO-5 catalyst. We contrast the behaviour of the monometallic CoAlPO-5 and bimetallic CoTiAlPO-5 active species to uncover the nature of the observed catalytic synergy. Specific emphasis is placed on the cobalt site, to provide complementary data to previous findings on the local environment of the titanium ions. By contrasting their behaviour in sustainable catalytic applications, we will now demonstrate the benefits of simultaneous incorporation of these two ions.[21]

Results and discussion

Cobalt K-edge EXAFS spectra were collected and analyzed to determine the local coordination environment of the active Co site in the calcined (catalytically active) and reduced states (Figure 1, Figure S2 and S3). It is known from previous studies that not all the cobalt sites in AlPO-5 framework can be raised to the trivalent oxidation state therefore a mixture of environments is expected. All four experimental EXAFS data sets corresponding to oxidized and reduced samples of the mono- and bi-metallic catalysts were modelled simultaneously using a similar set of parameters (Table S2). This model includes an oxygen shell and two phosphorus shells for the monometallic catalyst and a Ti shell substituted for one P shell for the bimetallic catalyst (Figure S4 and S5).

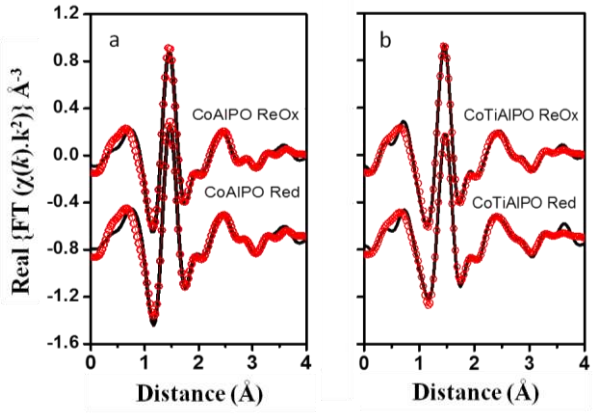

Figure 1. EXAFS data (black) and model (red with symbols) for oxidized (-Reox) and reduced (-Red) monoatomic CoAlPO (left) and bimetallic CoTiAlPO (right) samples, showing the real part of the Fourier Transform.

In both the monometallic (CoAlPO-5) and bimetallic (CoTiAlPO-5) catalysts the XANES (Figure S2) and EXAFS data indicate that cobalt is present in four-coordinate geometry, given that the EXAFS coordination number for Co-O shell is approximately 4 (Table 1), as expected for dopants undergoing type I substitution, (isomorphous incorporation into the AlPO framework, substituting an Al^{3+} ion). These findings are in excellent agreement with previous UV/Vis data on the system, which also confirms that the cobalt ions occupy a tetrahedral geometry (Figure S6).[16] Both the oxidised and reduced monometallic CoAlPO-5 samples showed possibility of mixed Co environments, as expected, due to the two oxidation states. The EXAFS model indicates the average Co-O bond length of 1.93 ± 0.01 Å for the oxidised catalyst, indicating a mixture of Co^{2+} and Co^{3+}, while the reduced sample shows an extended Co-O bond length of 1.95 ± 0.01 Å, indicating a greater fraction of Co^{2+}ions, in line with previous UV/Vis data (Figure S6).[16] The σ^2 factor (0.008 ± 0.001 $Å^2$) in the first shell Co-O indicate structural disorder, consistent with the mixed oxidation state environment.

Table 1. EXAFS parameters for monometallic CoAlPO-5 and bimetallic CoTiAlPO-5 catalyst samples.

Monometallic CoAlPO-5

	Oxidised			Reduced		
Path	CN	R/Å	σ^2 /x10^{-3} $Å^2$	CN	R/Å	σ^2 /x10^{-3} $Å^2$
Co-O1	3.7 ± 0.2	1.93 ± 0.01	8.1 ± 0.8	4.1 ± 0.2	1.95 ± 0.01	8.1 ± 0.8
Co-P1	2.7 ± 0.9	3.16 ± 0.02	13.4 ± 4.9	2.9 ± 1.0	3.16 ± 0.02	13.4 ± 4.9
Co-P2	1.6 ± 0.7	3.42 ± 0.01	13.4 ± 4.9	2.4 ± 0.9	3.42 ± 0.02	13.4 ± 4.9

Bimetallic CoTiAlPO-5

	Oxidised			Reduced		
Path	CN	R/Å	σ^2 /x10^{-3} $Å^2$	CN	R/Å	σ^2 /x10^{-3} $Å^2$
Co-O1	3.8 ± 0.2	1.93 ± 0.01	8.1 ± 0.8	3.5 ± 0.3	1.95 ± 0.01	8.1 ± 0.8
Co-P1	4.0 ± 1.3	3.16 ± 0.02	13.4 ± 4.9	4.1 ± 1.9	3.16 ± 0.02	13.4 ± 4.9
Co-Ti	2.5 ± 1.0	3.24 ± 0.02	13.4 ± 4.9	2.7 ± 1.7	3.24 ± 0.02	13.4 ± 4.9

In addition to the EXAFS modelling of the first shell, the second shell in the EXAFS spectra can be represented by split Co-P distance grouped at ~3.15 and ~3.4 Å as predicted by the AlPO structure and DFT (see below). Indeed, the existence of a next nearest neighbour peak at this distance corresponds well to published literature data for the Co-P distances of the 2nd coordination sphere[22] and is therefore consistent with framework incorporation at Al sites. The lack of appropriate contributions from Co-Co scattering path lengths (which would be expected to occur in the range of 2.9-3.3 Å for cobalt in an oxidic system) shows that the cobalt is isolated within the framework, and has not formed metal-oxide clusters. The presence of ~3.0 ± 1.0 P atoms at 3.16 Å, shown by EXAFS model (Table 1), is in agreement with the DFT calculation for AlPO structure predicting 3 P atoms between 3.09 and 3.19Å (see below). The spread in the bond distance of these P atoms results in a relatively large σ^2 value for P. At 3.4 Å, the EXAFS should ideally show 1 P atom but due to the presence of strong multiple scattering signals from mixed Co^{2+} and Co^{3+} environments (between 3.2 and 3.5Å) the EXAFS analysis is more complex in this region. Our modelling considers the inclusion of only single scattering signals (to reduce the added complexities often associated with the inclusion of multiple scattering signals) and results in ~ 2.5 ± 1.0 P atoms at 3.42 Å (Table 1). Consequently the CN and the associated uncertainty for the second P atom is higher than expected. The bimetallic catalyst spectra were modelled both by replacing the second Co-P scattering path with a Co-Ti path (Table 1) and also with the split P model (Table S3). While the models are statistically similar, the EXAFS data are consistent with the presence of a Co-Ti path in the bimetallic catalyst, and this is strongly supported by the DFT calculations detailed below. This finding supports the notion of adjacent bimetallic substitution, whereby cobalt has undergone a type I substitu-

tion mechanism (substituting Al^{3+}), whilst simultaneously titanium has undergone a type II substitution (isomorphous substitution into the AlPO framework to replace a P^{5+} ion), adjacent to the cobalt. This dopant cluster may modify the local structural strain relative to isolated dopant sites, leading to a different local environment of Co.

The ability of cobalt to undergo type I substitution (replacing Al^{3+}, as determined from the EXAFS results), and titanium to undergo type II substitution (replacing P^{5+}) was used as the basis to probe the active site(s) directly using computational chemistry methods. The lowest-energy geometries of monometallic (Co^{2+}, Co^{3+} and Ti^{4+}) and undoped AlPO-5 systems were calculated using periodic DFT calculations; full structural results are reported in the ESI. The structure of undoped AlPO-5, with lattice parameters a = b = 13.75 Å, c = 8.35 Å and individual Al-O and P-O bond lengths of 1.74 ± 0.02 and 1.54 ± 0.01 Å is in good agreement with literature values (Table S4 and S5).[22,24] On isomorphously substituting a Co^{2+} ion for Al^{3+} (and introducing the appropriate charge-balancing proton) both the high spin and low spin d^7 electronic configurations were investigated. The high-spin state was found to be the stable electronic state, as expected for a first row transition element four coordinated by electron donor ligands. Incorporation of Co^{2+} causes a local structural expansion relative to Al; the equilibrium structure contains three Co-O bonds of ~1.88 Å (1.87, 1.88 and 1.90 Å) and a significantly longer Co-OH bond to the protonated framework oxygen (2.12 Å, Table S6 and S7). An elongation of 0.1 Å or more of the bond distances between framework ions and protonated relative to non-protonated oxygen ions is invariably observed in all doped zeotypes.[24]

The oxidised Co^{3+} ion in a framework Al site is again stable in high-spin (d^6) electronic configuration. Its calculated equilibrium bond distances (Table S8) are shorter and more symmetric than those of Co^{2+}, due to the smaller ionic radius of Co^{3+} relative to Co^{2+}, and the absence of protonated oxygens in the first coordination shell of Co^{3+}. The Co-O distances calculated for the monometallic CoAlPO-5 systems, averaged over the 4 nearest neighbour oxygens of Co, are of 1.94 and 1.82 Å for Co^{2+} and Co^{3+} respectively, in agreement with the experimental EXAFS results (Table 1). The equilibrium Co-P distances in the second coordination shell of Co range between 3.096 and 3.196 Å, also in good agreement with those found experimentally from the EXAFS modelling (3.16 Å), confirming that type I substitution (Co^{2+} replacing a framework Al^{3+}) has occurred. Given the agreement of calculated and observed geometries, it follows that our computational model is appropriate for a quantitative description of the cobalt sites found experimentally.

In both Co^{2+} and Co^{3+} systems the oxygen ions nearest neighbour of Co show a small spin polarisation (see Tables S7 & S9), obtained by π donation from the oxide ions into the singly occupied d atomic orbitals of Co. The donation is higher for Co^{3+}, given its stronger Lewis acid character, resulting in a higher spin polarisation (of ~0.2|e|) on the oxygen ions bonded to Co^{3+} than those bonded to Co^{2+} (0.08|e|). Hydrocarbon oxidation reactions in metal-doped AlPOs initiate through a homolytic H-abstraction step from a framework O next to the dopant.[25,26] Increased spin polarisation on this oxygen facilitates the radical mechanism and therefore correlates with catalytic activity.

The monometallic Ti^{4+}AlPO-5 system was simulated by replacing a framework P^{5+} ion with Ti^{4+}, through type II substitution, in agreement with our previous UV/Vis data (Figure S6B). The equilibrium structure around Ti consists of three shorter Ti-O bonds (1.75, 1.77 and 1.78 Å, Table S10) whilst the protonated Ti-OH bond again shows a significant expansion (1.99 Å, Table S10). It is important to note that Ti causes a significant expansion relative to the framework P ion it replaces (whose P-O bond distances are of 1.54 Å). The electronic structure of Ti^{4+}AlPO-5 reveals no spin polarisation, consistently with the d^0 configuration of Ti^{4+} (Table S11).

Having characterized computationally the local environment of Co and Ti in the monometallic Me-AlPO-5 systems, we now discuss our findings when one Co (in either +2 or +3 oxidation state) and one Ti^{4+} ion are simultaneously incorporated in the same AFI unit cell. Apart from quantitatively interpreting the EXAFS results, our goal was also to identify similarities and differences in the geometry and electronic structure of mono- and bi-metallic materials, which can provide valuable insights into the synergic catalytic enhancement observed experimentally.[9,16] The first feature we have investigated is the configurational landscape of the co-doped material, i.e. the relative stability of Co and Ti ions located at different separation in the framework. The configurations examined include Co and Ti in nearest neighbour (adjacent) T sites and further apart in the structure (Table S12). In these initial calculations cobalt was purposefully limited to the divalent "as-synthesised" state, to represent the ions during the crystallisation stage, as this is the point at which the dopant location in the framework is determined. The relative stability of different (Co, Ti) configurations in the bimetallic catalyst is related to the energy of separated Co and Ti sites in the monometallic solids, through the definition of a clustering energy (E_{clu}) given by equation 1.

(Eq 1.) $E_{clu} = E[Co^{2+}Ti^{4+}AlPO\text{-}5] + E[AlPO\text{-}5] - E[Co^{2+}AlPO\text{-}5] - E[Ti^{4+}AlPO\text{-}5]$

where E[M(M')AlPO-5] are the calculated energies of one AlPO-5 unit cell containing the M (and M') dopants and E[AlPO-5] is the energy of one undoped unit cell. Negative clustering energies indicate stability of the bimetallic system relative to separate monometallic ones.

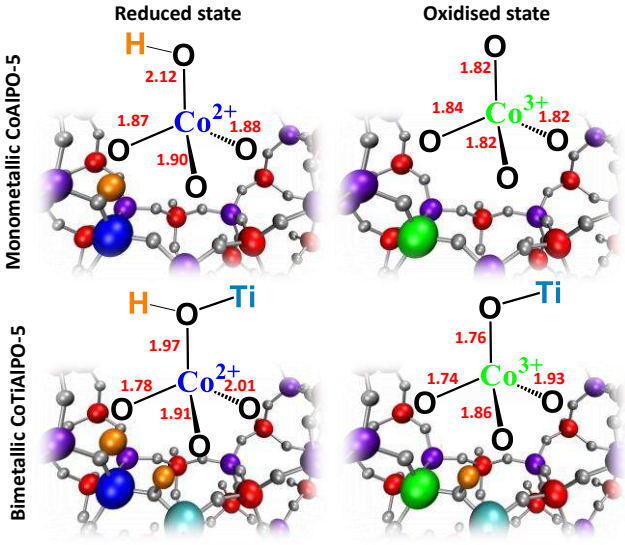

Figure 2. Calculated equilibrium bond distances for mono- and bi-metallic, oxidised and reduced cobalt sites.

Co^{2+} and Ti^{4+} ions each require one proton for charge balance. Binding one proton to one of the four nearest neighbour oxygens of both ions gives rise to 16 distinct proton distributions; all 16 have been examined explicitly for Co-Ti in adjacent T sites (Table S13) and further apart in the same unit cell of AlPO-5 (Table S14). The choice of protonation sites is critical, especially for the case of Co-Ti clustered in nearest T sites, where it accounts for a

variation of over 136 kJ/mol in the energy (Table S13). It is therefore essential to examine exhaustively the possible protonation sites. For each (Co, Ti) configuration, results in Table S12 are based on the most stable proton distribution. Clustering energies of Co^{2+} and Ti^{4+} are calculated to be negative for all bimetallic cells investigated, and there is a clear trend between proximity of Co to Ti and stability. The most stable configuration corresponds to Co and Ti in adjacent T sites, with clustering energy of -66.6 kJ/mol; Co and Ti in next-nearest T site configuration (i.e. forming a Co-P-Al-Ti unit) have instead a calculated clustering energy of -22.8 kJ/mol.

These results clearly indicate a thermodynamic preference for Co and Ti to be located in close proximity in the bimetallic catalyst, and in particular for adjacent bimetallic substitution of the two elements. During synthesis the likelihood of Co-O-Ti units forming is improved, thus we can expect a larger fraction of Co and Ti sites to be located in close proximity. This result further validates the EXAFS model used which includes a Co-Ti path, in the bimetallic catalyst which provides an atomic structure link to the observed catalytic synergy.

Analysis of the Co-O bond distances in the equilibrium structure calculated for adjacent Co-Ti sites in the bimetallic solid (Figure 2 and Tables S15 and S17) shows a subtly different structural environment than in the monometallic CoAlPO-5. In particular the bridging oxygen between Co and Ti ions has much shorter Co-O bond distance (1.97 vs 2.12 Å). We attribute this feature to the larger ionic radius of Ti^{4+} relative to P^{5+}, which can be equated to a local chemical pressure that compresses the adjacent Co-O(H) bond. When averaged over all four nearest neighbour oxygens, the EXAFS model showed both were 1.93 ± 0.01 Å. However, this average value may not be a significant parameter for the bimetallic solid, given the significant spread among the individual bond distances. When considering Co and Ti dopants in the same unit cell, but in non-adjacent T sites (Tables S19 and S21) we observe a local structure for Co^{2+} where three Co-O bonds are slightly longer than in the monometallic solid, and one considerably shorter, resulting in values averaged over the 4 nearest neighbours of 1.94 Å, the same as in the monometallic solid.

The fact that Co and Ti are most stable when in adjacent framework T sites deserves a more in-depth analysis. Both Co^{2+} and Ti^{4+} dopant ions require a lattice expansion relative to the undoped framework, hence clustering generates a build-up of steric strain, as demonstrated by the bond distances discussed above. Comparing the equilibrium structure around Co, it is evident that the chemical pressure generated by Ti in the local environment causes a substantial compression of the bridging Co-O bond. A possible rationale to explain the favourable clustering originates from the unique properties of the O ion bridging Co and Ti dopants in adjacent T sites. Analysis of calculated charges shows that this bridging oxygen is much more basic and more ionic than the oxygens directly bonded to P. The latter form acidic molecular orthophosphate (PO_4^{3-}) ions in AlPOs. The basicity of the Co-Ti bridging oxygen results in a more favourable protonation energy, and the ionicity in enhanced structural flexibility due to non-directional ionic bonding. The latter feature is demonstrated by the equilibrium Co-O-Ti angle of 111.68 degrees, which is much smaller than the Al-O-P angle (140.95°) in the undoped framework, but also smaller than Co-O-P (133.85°) and Al-O-Ti (130.17°) angles in the monometallic catalysts. The Co-O-P angle for Co near but not adjacent to Ti in the bimetallic solid has intermediate value of 126.30 degrees. The increased flexibility of the Co-O-Ti angle in the bimetallic catalyst contributes to absorb the steric strain caused by doping, hence stabilising the dopant clustering.

It is finally important to stress that all calculations reported in this study on the reduced bimetallic materials converged to $Co^{2+}Ti^{4+}$ electronic state, and, despite attempts to appropriately constrain the spin, we did not observe any evidence (under our conditions) for the existence of the isoelectronic $Co^{3+}Ti^{3+}$structure. Cobalt is therefore the redox-active ion in the bimetallic catalyst, while Ti serves the major goal of providing synergic activation of Co, while remaining itself in 4+ oxidation state throughout.

In order to draw meaningful comparisons with the behaviour of the monometallic species, equilibrium geometry and energy of the oxidised bimetallic $Co^{3+}Ti^{4+}$AlPO-5 catalyst were also calculated. We first consider the material containing the stable Co-O-Ti bridge. The geometries were derived from that of $Co^{2+}Ti^{4+}$AlPO-5, by removing either of the two protons. The lowest-energy configuration retained the proton associated with the titanium ion only, via loss of the proton bound to the oxygen of the Co-O-Ti bridge. The system with Co^{3+} and Ti^{4+} ions in adjacent T sites has a calculated clustering energy of -17.9 kJ/mol relative to isolated dopant ions, while Co^{3+} and Ti^{4+} ions in the same unit cell but non-adjacent have a calculated clustering energy of -8.3 kJ/mol. Also in the 3+ oxidation state, therefore, Co is stable when in proximity of Ti, although clustering energies are substantially smaller than for Co^{2+}.

As for Co^{2+}, the bridging oxygen between Co^{3+} and Ti ions has much shorter Co-O bond distances than in the monometallic Co-AlPO-5 material (1.76 vs 1.82 Å see Figure 2) due to the ionic size of the Ti. This is accompanied by a longer (1.93 Å) Co-O bond, so that the average over all four nearest neighbour oxygens is of 1.82 Å, unchanged relative to the monometallic solid. When considering Co and Ti in non-adjacent T sites (Table S21) we observe a local structure where three Co-O bonds are slightly longer than in the monometallic solid, and one considerably shorter, resulting in values averaged over the 4 nearest neighbours of 1.82 Å, again the same as in the monometallic solid.

Table 2. Comparison of calculated and experimental Co-O bond lengths.

Monometallic CoAlPO-5 distances/Å			
DFT Co^{II}-O	1.94	DFT Co^{III}-O	1.82
EXAFS Reduced Co-O	1.95	EXAFS Oxidised Co-O	1.93
Bimetallic CoTiAlPO-5 distances/Å			
DFT Co^{II}-O	1.92	DFT Co^{III}-O	1.82
EXAFS Reduced Co-O	1.95	EXAFS Oxidised Co-O	1.93

The calculated energies for the mono- and bi-metallic materials in oxidised and reduced forms can be combined to evaluate the reduction energy (+3/+2) of Co in the catalysts, via Eq 2 and 3 below:

(Eq.2) $\Delta E = E[Co^{2+}AlPO\text{-}5] - E[Co^{3+}AlPO\text{-}5] - E[H_2]/2$

(Eq.3) $\Delta E = E[Co^{2+}Ti^{4+}AlPO\text{-}5] - E[Co^{3+}Ti^{4+}AlPO\text{-}5] - E[H_2]/2$

where $E[H_2]$ is the energy of a gas phase hydrogen molecule calculated consistently with that of the solid catalysts. ΔE is intrinsically linked to the catalytic activity of MeAlPOs in selective oxidation reactions, where the reduction of the metal from +3 to +2 occurs in the rate limiting steps.[25,26]

The reduction energy of Co in the monometallic CoAlPO-5 material is calculated to be -1.23 eV/ion, corresponding to a standard

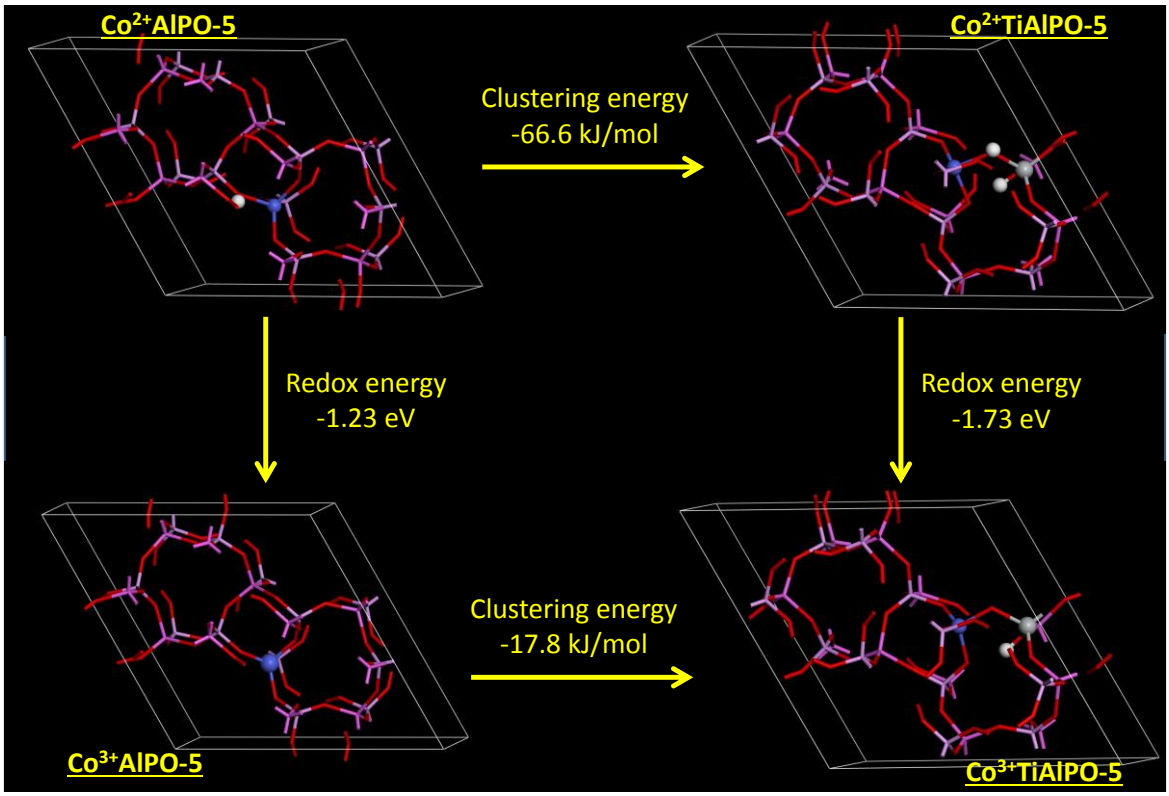

Figure 3. Reduction energy of Co^{3+} with molecular hydrogen in monometallic and bimetallic materials.

reduction potential of 1.23 V (Figure 3). This value is lower than other cobalt-substituted AlPO materials,[24] indicating greater preference for the divalent over the trivalent state, and in good agreement with previous studies that showed the redox fraction in CoAlPO-5 to be lower than in most other AlPO structures.[22] The equivalent reduction energy is -1.73 eV/ion for Co adjacent to Ti in the bimetallic CoTiAlPO-5 system (Figure 3). The bimetallic species favours therefore the divalent state to a greater extent than the monometallic system, and may thus be expected to be more catalytically active. By contrasting the calculated clustering energies for +2 and +3 oxidation states of cobalt in mono- and bimetallic solids, we conclude that the higher reduction potential of Co is to be attributed to a higher stabilisation of the divalent state relative to the trivalent in the bimetallic solid, resulting in favourable reduction.

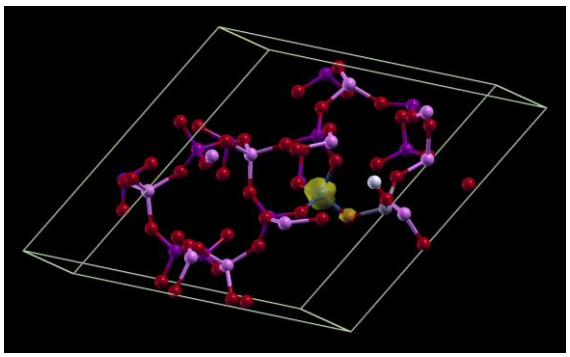

Figure 4. Spin density plot of $Co^{3+}Ti^{4+}$AlPO-5 , containing adjacent Co(blue) and Ti(grey) ions, highlighting the high spin polarisation of the Co-O-Ti bridging oxygen.

It is important to note at this stage that despite the higher reduction potential, a fraction of cobalt is still raised to the Co^{3+} state during calcination in the bimetallic solid, accounting for the colour change from blue (pre-calcinaton) to green (post-calcination).

It is not only the geometry, but also the electronic structure of the oxygen ion bridging adjacent Co and Ti ions that is substantially different from the monometallic systems. The spin polarisation of this oxygen in the oxidised catalyst, of 0.419|e| (Table S18), is much higher than in the monometallic solid (0.218 |e|, Table S8). The spin polarisation is highlighted in Figure 4. The unique environment of the bridging oxygen directly bonded to two transition metal ions, enables effective spin delocalisation from Co^{3+} to Ti^{4+} through super-exchange interaction, the mechanism responsible for magnetic coupling in transition metal oxides, but unavailable for main group elements. Since selective oxidation reactions in metal-doped AlPOs proceed via radical abstractions of hydrogen atoms from the hydrocarbon substrates[25,26], it is not unreasonable to expect the spin polarisation of the bridging oxygen to be associated with higher activity, given the increased stabilization of the oxidised trivalent state, relative to the reduced divalent state. The transition between which is fundamental to the activity of these materials. If the correlation between spin polarisation and activity could be confirmed in a broader range of bimetallic solids, we would have identified a molecular descriptor able to represent catalytic activity, suitable for rational computational screening of new catalysts.

Conclusion

In summary, we have explored the synergic catalytic enhancement displayed by the bimetallic CoTiAlPO-5 system, in sustainable oxidation reactions, with particular emphasis on the isomorphously substituted, tetrahedral $Co^{2+/3+}$ active site, and its implicit role in the catalytic process. Co is the redox-active ion in the bimetallic catalyst, with Ti providing synergic activation, while

remaining itself in +4 oxidation state throughout. The synergistic catalytic enhancement of the bimetallic system can be explained on the basis of the thermodynamic stability of the Co and Ti ions towards clustering, which leads to a significant amount of Co and Ti ions being located in adjacent T sites, as evidenced through both computational chemistry and experimental spectroscopic findings. This adjacent substitution forces subtle changes in the local structural environment and electronic structure of the cobalt site, which translate into significant modifications of the redox behaviour, which is crucial for enhanced catalytic performance in selective oxidation reactions. We have further demonstrated that the stability of cobalt in its divalent oxidation state is further augmented in the bimetallic catalyst, prompting a more energetically favourable rate-determining step in the oxidation reactions, which can help explain the observed synergies in catalytic performance.

Experimental section

EXAFS modelling

The EXAFS spectra were modelled using ARTEMIS[28] and FEFF6.0[29] for the theoretical calculations based on crystal structures obtained by DFT calculations in this study. For monometallic CoAlPO, the EXAFS models include single scattering O paths with Co-O distances of 1.87 Å and two single scattering P path with Co-P distance of 3.1 and 3.4 Å. For bimetallic CoTiAlPO, the EXAFS model replaced one Co-P signal with a scattering path from Ti with a distance from Co of around 3.26 Å (resulting from a Co-O-Ti entity). There are 11 parameters used to describe the monometallic and bimetallic models listed in Table 1: 4 coordination numbers (CN), 4 change in path length (ΔR), 2 mean square displacement of the half path length values (σ^2), and an energy shift parameter (ΔE). The value for S_0^2 (0.82 ± 0.05) was determined from Co foil. The data range from 2.5 to 9.5 $Å^{-1}$ was used in the Fourier transform (FT) with k-weights of 1 and 2. The model was applied to the FT range of 1.0 to 3.5 Å. The EXAFS data and model is shown in Figure S4. All 4 data sets were modelled simultaneously. This dramatically increases the information content in the data to 40 independent points and 20 parameters.

Computational details

Electronic structure calculations were performed on the University of Southampton Iridis3 supercluster with the CRYSTAL09 periodic DFT code[29] using the B3LYP hybrid-exchange functional.[30-34] The AFI framework was calculated using periodic boundary conditions in P1 space group to allow full-optimisation without symmetry constraints. The electronic distribution was described as a linear combination of atomic orbitals and the basis functions are expressed as Gaussian-type orbitals. Aluminium, phosphorus, oxygen and hydrogen ions were described using a double valence plus polarization basis set whereas titanium and cobalt were described using a triple-valence plus polarization basis set. All basis sets employed were taken from the online library for the CRYSTAL code.[35] The AFI structure was described by modelling one unit cell containing 72 atoms (12 $AlPO_4$ formula units). Cobalt was substituted for aluminium and titanium was substituted for phosphorus. In the case of a charge imbalance (Co^{2+} substituting Al^{3+} or Ti^{4+} substituting for P^{5+}) a proton was attached to an oxygen ion adjacent to the divalent or tetravalent dopant. One substitution was made per metal per unit cell, corresponding to 8.3 mol% loading.

ASSOCIATED CONTENT

Supporting Information

Supporting information is available where further experimental, computational, mechanistic and catalytic data can be found. This material is available free of charge via the Internet at http://pubs.acs.org.

AUTHOR INFORMATION

Corresponding Author

MEP: matthew.potter@chbe.gatech.edu
RR: R.Raja@soton.ac.uk

Notes

The authors declare no competing financial interests.

ACKNOWLEDGMENT

We acknowledge Honeywell LLC for financial support. Use of the Advanced Photon Source, an Office of Science User Facility operated for the U.S. Department of Energy (DOE) Office of Science by Argonne National Laboratory, was supported by the U.S. DOE under Contract No. DE-AC02-06CH11357. MRCAT operations are supported by the Department of Energy and the MRCAT member institutions.

REFERENCES

1 Maschmeyer, T.; Rey, F.; Sankar, G.; Thomas, J. M. *Nature*, **1995**, *378*, 159-162.
2 Bell, A. T. *Science*, **2003**, *299*, 1688-1691.
3 Lee, J.; Farha, O. K.; Roberts, J.; Scheidt, K. A.; Nguyen, S. T.; Hupp, J. T. *Chem. Soc. Rev.*, **2009**, *38*, 1450-1459.
4 Oldroyd, R. D.; Thomas, J. M.; Sankar, G. *Chem. Commun.*, **1997**, *21*, 2025-2056.
5 Corma, A.; Nemeth, L. T.; Renz, M.; Valenica, S. *Nature*, **2001**, *412*, 423-425.
6 Kesavan, L.; Tiruvalam, R.; Ab Rahim, M. H.; bin Saiman, M. I.; Enache, D. I.; Jenkins, R. L.; Dimitratos, N.; Lopez-Sanchez, J. A.; Taylor, S. H.; Knight, D. W.; Kiely, C. J.; Hutchings, G. J. *Science*, **2011**, *331*, 195-199.
7 Hungaria, A. B.; Raja, R.; Adams, R. D.; Captain, B.; Thomas, J. M.; Midgley, P. A.; Golovoko V.; Johnson, B. F. G. *Angew. Chem. Int. Ed.,* **2006**, *45*, 4782-4785.
8 Gianotti, E.; Manzoli, M.; Potter, M. E.; Shetti, V. N.; Sun, D.; Paterson, A. J.; Mezza, T.; Levy, A. B.; Raja, R. *Chem. Sci.*, **2014**, *5*, 1810-1819.
9 Leithall, R. M.; Shetti, V. N.; Maurelli, S.; Chiesa, M.; Gianotti, E.; Raja, R. *J. Am. Chem. Soc.*, **2013**, *135*, 2915-2918.
10 Thomas, J. M.; Sankar, G. *Acc. Chem. Res.*, **2001**, *34*, 571-581.
11 O'Brien, M. G.; Beale, A. M.; Jacques, S. D. M.; Di Michiel, M.; Weckhuysen, B. M. *Appl. Catal. A-Gen.*, **2011**, *391*, 468-476.
12 Arean, C. O.; Weckhuysen, B. M.; Zecchina, A. *Phys. Chem. Chem. Phys.*, **2012**, *14*, 2125-2127.
13 Lamberti, C.; Bordiga, S.; Bonino, F.; Prestipino, C.; Berlier, G.; Capello, L.; D'Acapito, F.; Xamena, F. X. L. I.; Zecchina, A. *Phys. Chem. Chem. Phys.*, **2003**, *5*, 4502-4509.
14 Bartlett, S. A.; Wells, P. P.; Nachtegaal, M.; Dent, A. J.; Cibin, G.; Reid, G.; Evans, J.; Tromp, M. *J. Catal.*, **2011**, *284*, 247-258.
15 Gilson, J. P.; Fernandez, C.; Thibault-Starzyk, F. *J. Mol. Catal. A-Chem.*, **2009**, *305*, 54-59.
16 Paterson, A. J.; Potter, M. E.; Gianotti, E.; Raja, R. *Chem. Commun.*, **2011**, *47*, 517-519.
17 Thomas, J. M.; Raja, R.; Lewis, D. W. *Angew. Chem. Int. Ed.*, **2005**, *44*, 6456-6482.
18 Thomas, J. M.; Raja, R. Annu. Rev. Mater. Res., **2005**, *35*, 315-350.
19 Potter, M. E.; Sun, D.; Gianotti, E.; Manzoli, M.; Raja, R. *Phys. Chem. Chem. Phys.*, **2013**, *15*, 13288-13295.
20 Lefenfeld, M.; Raja, R.; Paterson, A. J.; Potter, M. E. *US Patent* 021882, **2010**.

21 Thomas, J. M.; Raja, R. *Proc. Natl. Acad. Sci.*, **2005**, *39*, 13732-13736.
22 Sankar, G.; Raja, R.; Thomas, J. M. *Catal. Lett.*, **1998**, *55*, 15-23.
23 Lee, S. O.; Raja, R.; Harris, K. D. M.; Thomas, J. M.; Johnson, B. F. G.; Sankar, G. *Angew. Chem. Int. Ed.*, **2003**, *115*, 1558-1561.
24 Cora, F.; Alfredsson, M.; Barker, C. M.; Bell, R. G.; Foster, M. D.; Saadoune, I.; Simplerer, A.; Catlow, C. R. A. *J. Solid State Chem.*, **2003**, *176*, 496-529.
25 Gomez-Hortiguela, L.; Cora, F.; Sankar, G.; Zicovich-Wilson, C. M.; Catlow, C. R. A. *Chem. Eur J.*, **2010**, *16*, 13638-13645.
26 Gomez-Hortiguela, L.; Cora, F.; Catlow, C. R. A. *ACS Catal.*, **2011**, *1*, 18-28.
27 Cora, F; Catlow, C. R. A. *J. Phys. Chem. B*, **2001**, *105*, 10278-10281.
28 Rehr, J. J.; Kas, J. J.; Prange, M. P.; Sorini, A. P.; Takimoto, Y.; Villa, F. *C. R. Physique*, **2009**, *10*, 548-559.
29 Newville, M.; Ravel, B.; Haskel, D.; Rehr, J. J.; Stern, E. A.; Yacoby, Y. *Physica B.*, **1995**, *208*, 154-156.
30 Dovesi, R.; Orlando, R.; Civalleri, B.; Roetti, C.; Saunders, V. R.; Zicovich-Wilson, C. M. *Z. Kristallogr.*, **2005**, *220*, 571-573.
31 Becke, A. D. *J. Phys. Chem.*, **1993**, *98*, 5648-5652.
32 Lee, C.; Yang, W.; Parr, R. G. *Phys. Rev. B*, **1988**, *37*, 785-789.
33 Vosko, S. H.; Willk, L.; Nusair, M. *Can. J. Phys.*, **1980**, *58*, 1200-1211.
34 Stephens, P. J.; Devlin, F. J.; Chabalowski, C. F.; Frisch, M. J. *J. Phys. Chem.*, **1994**, *98*, 11623-11627.
35 CRYSTAL Basis Sets Library. (http://www.crystal.unito.it/Basis_Sets/Ptable.html) accessed November 2011.

Insert Table of Contents artwork here

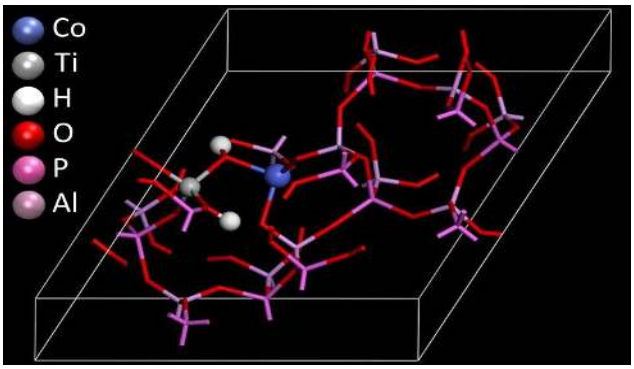

SUPPLEMENTARY INFORMATION

Spectroscopic and computational insights on catalytic synergy in bimetallic aluminophosphate catalysts

Matthew E. Potter,[a,b]* A. James Paterson,[b] Bhoopesh Mishra,[c] Shelly Kelly,[d] Simon R. Bare,[d] F. Cora,[e] Alan B. Levy[f] and Robert Raja[b]*

[a] Department of Chemical and Biochemical Engineering, Georgia Institute of Technology, 311 Ferst Drive, Atlanta, GA 30332, USA. E-mail: matthew.potter@chbe.gatech.edu.

[b] School of Chemistry, University of Southampton, Southampton, Hampshire, United Kingdom, SO17 1BJ. *Fax: 02380 592144; Tel: 02380 593781; E-mail: R.Raja@soton.ac.uk.

[c] Physics Department, Illinois Institute of Technology, Chicago, IL, 60016, USA.

[d] UOP LLC, A Honeywell Company, 25 East Algonquin Road, Des Plaines, IL 60017, USA.

[e] Department of Chemistry, University College London, 20 Gordon Street, London WC1H 0AJ, UK.

[f] Honeywell Int, 101 Columbia Road, Morristown, NJ 07962, USA.

Table of contents

Previous catalytic data with CoTiAlPO-5

Table S1: Catalytic data for cyclohexene epoxidation, taken from reference 1.

Catalyst	Conversion/mol%	Selectivity/mol%	Turnover number
CoAlPO-5 monometallic	12.6	> 99	12.1
TiAlPO-5 monometallic	35.9	> 99	22.8
Co/TiAlPO-5 physical mixture	47.0	> 99	34.1
CoTiAlPO-5 bimetallic	82.0	> 99	49.1

Conditions: 313 mmol of DCM (solvent), 9.0 mmol of Triglyme (internal standard), 5.75 g of acetylperoxyborate (3.9 wt% peracetic acid content), 20 ml of H_2O (solvent), 9.25 mmol of cyclohexene and 0.25 g of fresh catalyst were mixed under reflux in a glass-lined reactor at 65 °C for 3 hours.

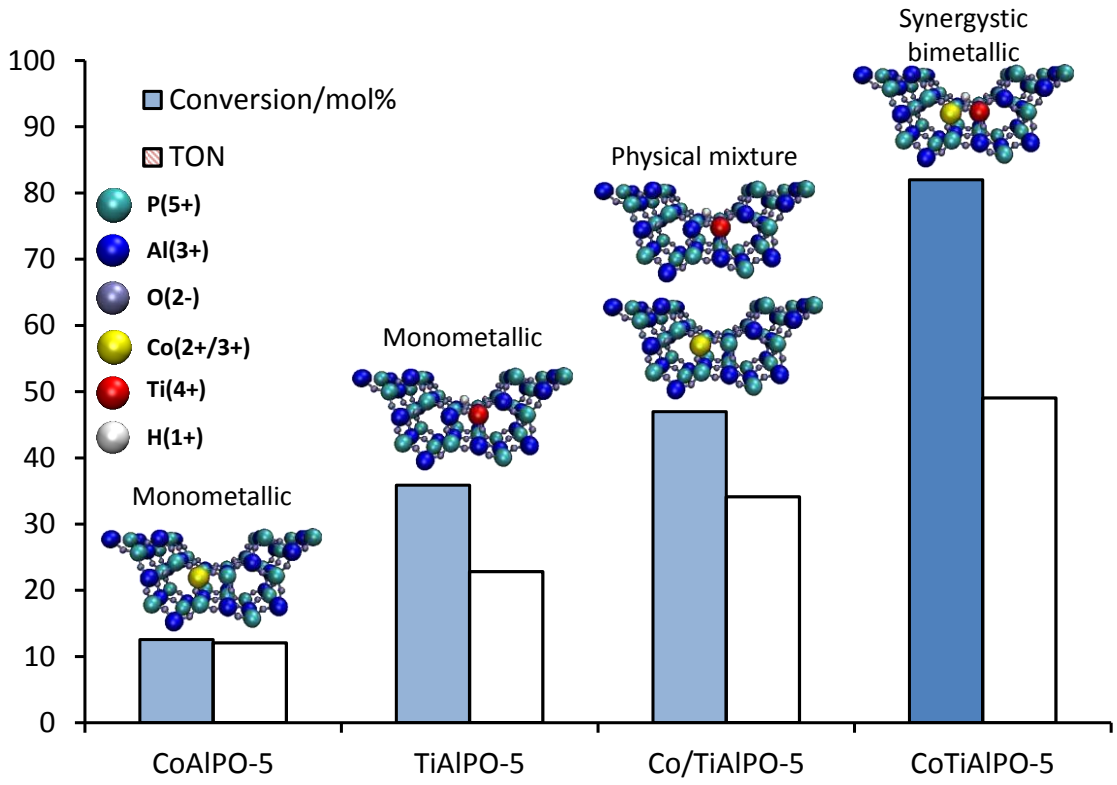

Figure S1: Catalytic synergy in the epoxidation of olefins[1] using monometallic and bimetallic Co(III) and Ti(IV) active centers, isomorphously incorporated into the AlPO-5 framework.

Experimental

Synthesis

The materials were synthesised using previously published procedures.[1] In summary the synthesis method of CoTiAlPO-5 involved mixing aluminium hydroxide hydrate (Aldrich) to a homogeneous solution of phosphoric acid (85% in H2O, Aldrich) in water. An aqueous solutions of cobalt(II) acetate tetrahydrate (Aldrich) and titanium isopropoxide (Aldrich) were added simultaneously. An aqueous solution of N,N-methyldicyclohexylamine (SDA) (Aldrich) was then added slowly with vigorous

stirring to obtain a black gel with the composition 0.96Al: 1.50P: 0.80MDCHA: 50H_2O: 0.03Co: 0.03Ti. The gel was sealed in a Teflon-lined stainless steel autoclave and heated at 180 ^oC under autogeneous pressure for 2 hr. The blue solid product was obtained by filtration, washed with deionised water, and dried in air. The as-prepared sample was calcined under a flow of air at 550 ^oC for 12 hr yielding a green sample. Similarly CoAlPO-5 was synthesised with the gel ratio of 0.96Al: 1.50P: 0.8MDCHA: 40H_2O: 0.04Co and crystallised for 2 hours at 200 ^oC. This was calcined at 550 ^oC for 12 hours again yielding a green sample.

EXAFS

The catalyst was calcined prior to the *in situ* XAFS experiments to remove the template and then cycled through an oxidation1-reduction-oxidation2 cycle *in situ* using a custom designed XAFS cell[2]. Approximately 35 mg of ground catalyst powder, for each sample, was pressed into a 4-hole sample holder. The two samples in the holder were loaded into the reactor together so that they were treated at the same time. The samples were translated into the x-ray beam sequentially so that data could be collected from both samples. The oxidation1-reduction-oxidation2 cycle details are given as follows. Oxidation 1: ramp to 150°C at 5°C/min in 20% O_2/He and hold for 30 min, followed by cool to RT. Reduction: ramp to 500°C at 5°C/min in 100% H_2 and hold for 30 min, followed by cool to RT. Oxidation 2: ramp to 500°C at 5°C/min in 20% O_2/He and hold for 30 min, followed by cool to 150°C. The EXAFS spectra were collected after this oxidation1-reduction-oxidation2 cycle at 150°C in 20% O_2/He.

EXAFS spectra were collected in transmission mode at the MR-CAT beamline 10ID at the Advanced Photon Source at Argonne National Laboratory. The insertion device x-ray beam was defined to be approximately 1mm in both the vertical and horizontal. A double crystal monochromator with Si(111) crystals was used to select the incident X-ray energy. X-rays of higher harmonic energies were minimized using a Rh-coated mirror. The x-ray energy was calibrated using a Co foil, which was also collected with the measured data by using a reference ionization chamber. The ionization chamber gasses were optimized using 20/80 mixture of N_2/He for the incident x-ray intensity and 100% N_2 for the transmitted and reference x-ray intensity measurements.

Further EXAFS and UV/Vis analysis

The EXAFS data were initially modelled with a Co-O and split Co-P shells (Table S2). The best-fit values for this model are listed in Table S3 and the real part of the FT of the EXAFS spectra are shown in Figure S2. The goodness-of-fit parameters including the Reduced-Chi-Square (RCS) is 529 and the R-factor is 0.32%. Then the model was modified to include Co-Ti path rather than one of the Co-P paths. The best-fit values for this model and the EXAFS spectra are shown in the main text (Table 1, and Figure 1). This model has similar statistical quality with RCS of 596 and R-factor of 0.35%.

Table S2: EXAFS model parameterisation

Neighbor	**R (Å)**	**CN**	**ΔR (Å)**	**σ^2 (Å^2)**
Co-O1	1.87	NO1	ΔRO1	σ^2O
Co-P1	3.10	NP1	ΔRP1	σ^2P

Co-Ti1*	3.26	NTi1	ΔRTi1	σ^2P
Co-P2*	3.42	NP2	ΔRP1	σ^2P

*Co-Ti1 path was substituted for Co-P2 in the CoTiAlPO samples. The two P shells were used for the CoAlPO samples.

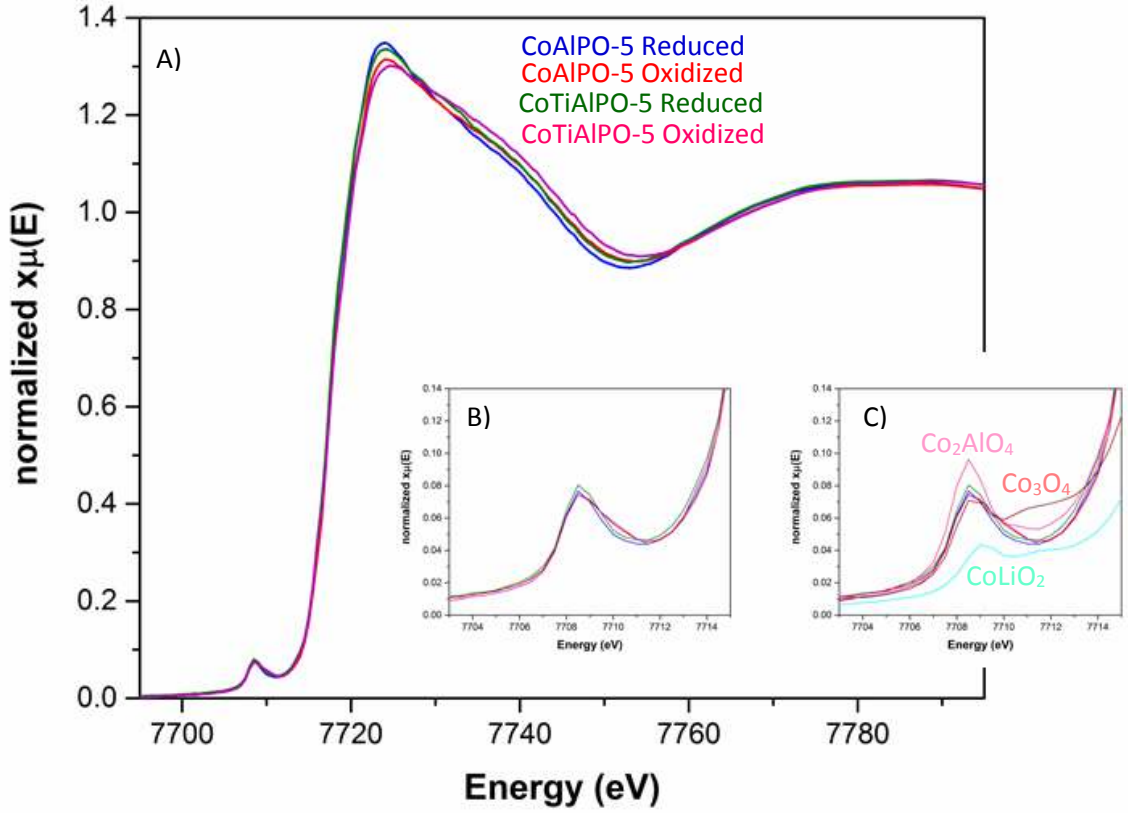

Figure S2: A) Detailing the XANES region of the catalysts in both the reduced and oxidized state. Positon of the pre-edge peak (B) is in excellent agreement with similar tetrahedral systems (C).

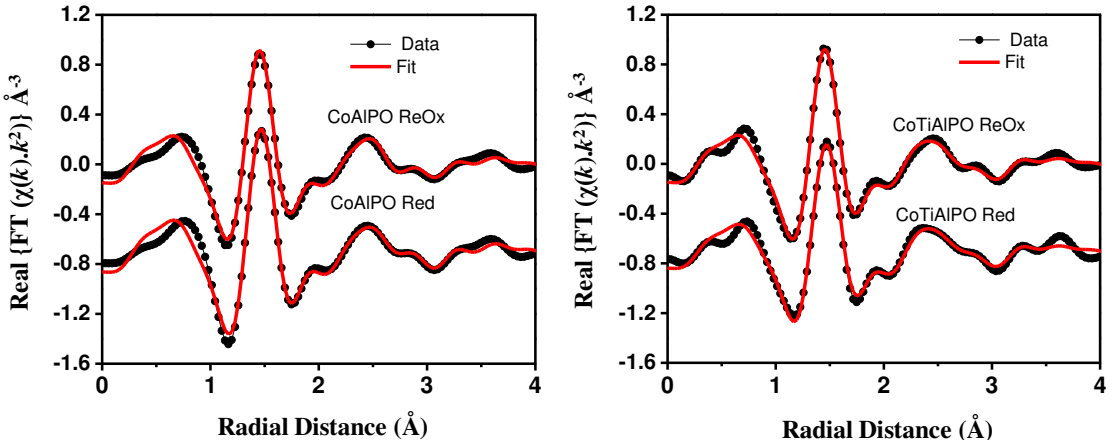

Figure S3: Real part of Fourier transform of the EXAFS spectra and model. All 4 data sets were simultaneously fit with three shell model (Co-O, Co-P1, and Co-P2). The RCS is 529 and the R-factor is 0.32%.

Table S3: EXAFS results for simultaneous fit to all 4 data sets with three shell model.

Path	N	R (Å)	σ^2 *10^{-3}(Å^2)
Reoxidized CoAlPO			
Co-O1	3.8 ± 0.2	1.93 ± 0.01	8.3 ± 0.8
Co-P1	2.8 ± 0.8	3.15 ± 0.02	13.8 ± 4.3
Co-P2	1.9 ± 0.7	3.42 ± 0.02	13.8 ± 4.3
Reduced CoAlPO			
Co-O1	4.1 ± 0.2	1.95 ± 0.01	8.3 ± 0.8
Co-P1	2.9 ± 0.9	3.15 ± 0.02	13.8 ± 4.3
Co-P2	2.6 ± 0.9	3.42 ± 0.02	13.8 ± 4.3
Reoxidized CoTiAlPO			
Co-O1	3.8 ± 0.2	1.93 ± 0.01	8.3 ± 0.8
Co-P1	3.0 ± 1.0	3.15 ± 0.02	13.8 ± 4.3
Co-P2	2.3 ± 0.9	3.42 ± 0.02	13.8 ± 4.3
Reduced CoTiAlPO			
Co-O1	3.9 ± 0.3	1.95 ± 0.01	8.3 ± 0.8
Co-P1	3.2 ± 1.3	3.15 ± 0.02	13.8 ± 4.3
Co-P2	2.8 ± 1.3	3.42 ± 0.02	13.8 ± 4.3

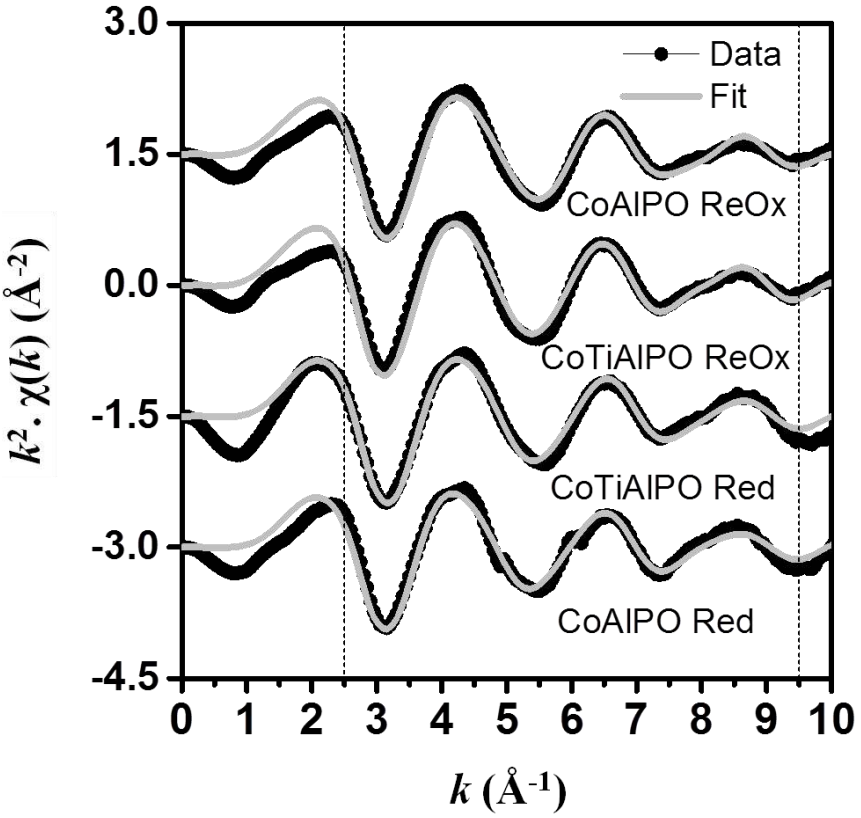

Figure S4: Experimental EXAFS (Black) and theoretical (Grey) data for $k^2 \bullet \chi(k)$ part of the Fourier Transform. The model includes Co-Ti shell for bimetallic catalyst samples.

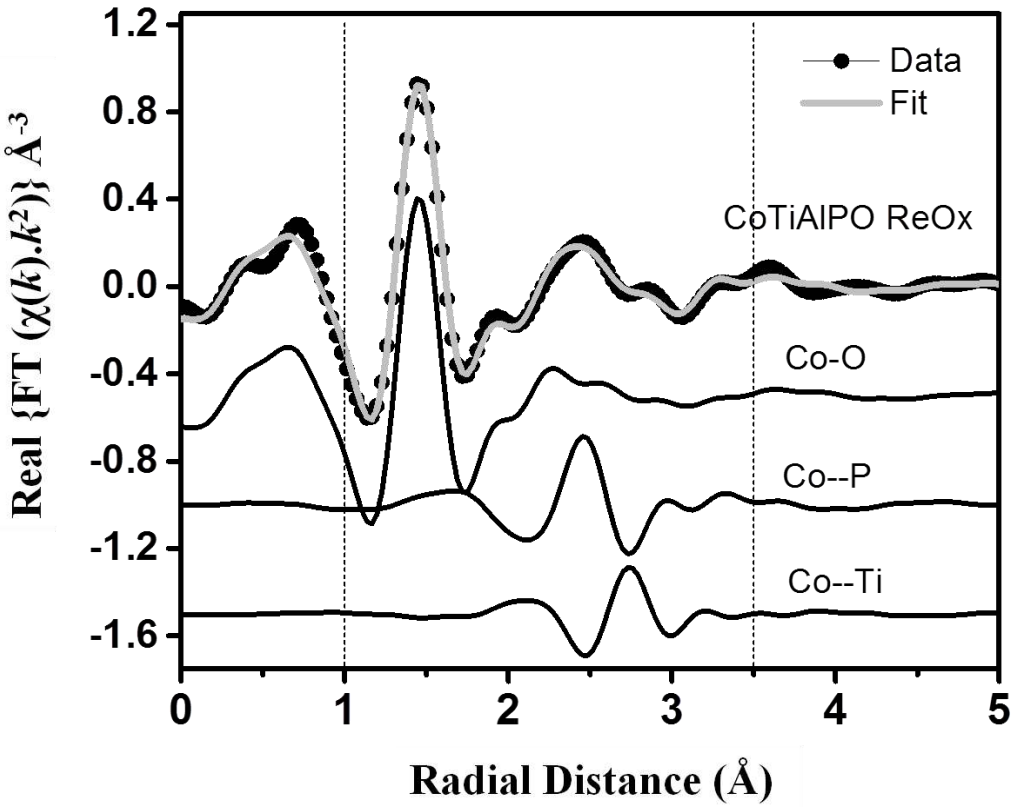

Figure S5: Data and fit for the real part of EXAFS Fourier Transform (FT) of reduced bimetallic CoTiAlPO sample, showing contribution of different signals in the model required to fit the data.

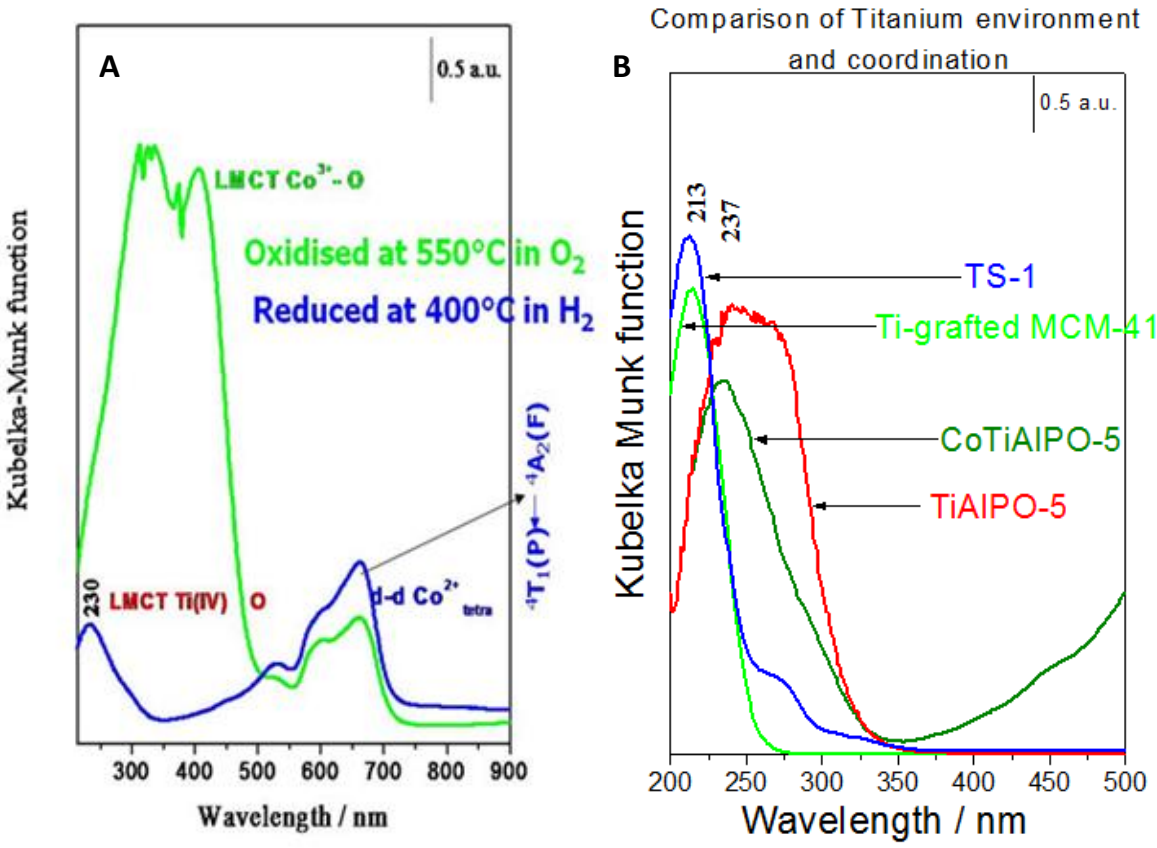

Figure S6: A) DR UV-Vis spectrum of calcined and reduced CoTiAlPO-5 showing characteristic tetrahedral Co^{2+} and Co^{3+} species. B) Contrasting Ti-O LMCT bands of known Ti-containing materials shows the tetrahedral nature of the titanium.

Cobalt shows two strong absorptions in the 250-500 nm range due to LMCT transitions between the oxygen ligands and the tetrahedral Co^{3+} sites. In the visible region, the triplet bands observed at 530, 592 and 659 nm can be assigned to the d-d transitions of Co^{2+} ions in Td coordination. The presence of this triplet after calcination, suggests that only a fraction of Co^{2+} ions can be oxidized to Co^{3+} state, which is consistent with the earlier observations.

Upon reduction in H_2 at 400°C, these strong absorptions associated with Co^{3+} ions completely disappear and a distinct band at 230 nm becomes apparent. This latter band can be assigned to isolated tetrahedral Ti^{4+} LMCT transitions. It is also noteworthy that this absorption is shifted to a higher wavelength and becomes slightly broader in the monometallic Ti^{4+}AlPO-5 catalyst, when compared with the bimetallic $Co^{3+}Ti^{4+}$AlPO-5 analogue.

Further computational details

Further computational data on undoped AlPO-5

Table S4: Bond lengths in undoped AlPO-5.

Atom 1	Atom 2	Bond length/Å
Al1	O1	1.736
Al1	O2	1.743
Al1	O3	1.738
Al1	O4	1.756
O1	P1	1.546
O2	P2	1.537
O3	P3	1.540
O4	P4	1.538
Al1	P1	3.077
Al1	P2	3.089
Al1	P3	3.082
Al1	P4	3.055

Table S5: Calculated Mulliken populations for undoped AlPO-5

Atom	Placement	Electron count (α + β)	Electron spin (α – β)
Al1	Central atom	11.057	0.000
O1	First coordination shell (Al1)	9.041	0.000
O2	First coordination shell (Al1)	9.047	0.000
O3	First coordination shell (Al1)	9.048	0.000

O4	First coordination shell (Al1)	9.044	0.000
P1	Second coordination shell (O1)	12.769	0.000
P2	Second coordination shell (O2)	12.761	0.000
P3	Second coordination shell (O3)	12.770	0.000
P4	Second coordination shell (O4)	12.770	0.000

Further computational data on monometallic Co^{2+}AlPO-5

Table S6: Bond lengths in monometallic Co^{2+}AlPO-5.

Atom 1	**Atom 2**	**Bond length/Å**
Co1	O1 (H1)	2.120
Co1	O2	1.871
Co1	O3	1.897
Co1	O4	1.876
O1 (H1)	P1 (H1)	1.608
O2	P2	1.518
O3	P3	1.520
O4	P4	1.524
Co1	P1 (H1)	3.424
Co1	P2	3.119
Co1	P3	3.100
Co1	P4	3.196
O1	H1	0.992
Co1	H1	2.652

Table S7: Calculated Mulliken populations for monometallic Co^{2+}AlPO-5

Atom	**Placement**	**Electron count (α + β)**	**Electron spin (α – β)**
Co1	Central atom	25.402	0.000
O1 (H)	First coordination shell (Co1)	8.890	0.023
O2	First coordination shell (Co1)	9.076	0.082
O3	First coordination shell (Co1)	9.085	0.070
O4	First coordination shell (Co1)	9.082	0.080
P1 (H)	Second coordination shell (O1)	12.742	0.002
P2	Second coordination shell (O2)	12.795	0.005
P3	Second coordination shell (O3)	12.781	0.007
P4	Second coordination shell (O4)	12.795	0.006
H1	Proton (O1)	0.634	0.000

Further computational data on monometallic Co^{3+}AlPO-5

Table S8: Bond lengths in monometallic Co^{3+}AlPO-5.

Atom 1	Atom 2	Bond length/Å
Co1	O1	1.816
Co1	O2	1.820
Co1	O3	1.837
Co1	O4	1.822
O1	P1	1.548
O2	P2	1.545
O3	P3	1.541
O4	P4	1.546
Co1	P1	3.139
Co1	P2	3.096
Co1	P3	3.143
Co1	P4	3.130

Table S9: Calculated Mulliken populations for monometallic Co^{3+}AlPO-5

Atom	Placement	Electron count (α + β)	Electron spin (α – β)
Co1	Central atom	25.106	3.071
O1	First coordination shell (Co1)	9.041	0.218
O2	First coordination shell (Co1)	9.042	0.218
O3	First coordination shell (Co1)	9.045	0.199
O4	First coordination shell (Co1)	9.053	0.203
P1	Second coordination shell (O1)	12.765	0.004
P2	Second coordination shell (O2)	12.771	0.003
P3	Second coordination shell (O3)	12.760	0.003
P4	Second coordination shell (O4)	12.761	0.003

Further computational data on monometallic Ti^{4+}AlPO-5

Table S10: Bond lengths in monometallic Ti^{4+}AlPO-5.

Atom 1	Atom 2	Bond length/Å
Ti1	O1 (H1)	1.987
Ti1	O2	1.775
Ti1	O3	1.765
Ti1	O4	1.751
O1 (H1)	Al1 (H1)	1.792

O2	Al2	1.700
O3	Al3	1.711
O4	Al4	1.751
Ti1	Al1 (H1)	3.425
Ti1	Al2	3.197
Ti1	Al3	3.284
Ti1	Al4	3.362
O1	H1	0.970
Ti1	H1	2.528

Table S11: Calculated Mulliken populations for monometallic Ti^{4+}AlPO-5

Atom	**Placement**	**Electron count (α + β)**	**Electron spin (α – β)**
Ti1	Central atom	19.985	0.000
O1 (H)	First coordination shell (Ti1)	8.934	0.000
O2	First coordination shell (Ti1)	9.062	0.000
O3	First coordination shell (Ti1)	9.077	0.000
O4	First coordination shell (Ti1)	9.050	0.000
Al1 (H)	Second coordination shell (O1)	11.058	0.000
Al2	Second coordination shell (O2)	11.081	0.000
Al3	Second coordination shell (O3)	11.062	0.000
Al4	Second coordination shell (O4)	11.070	0.000
H1	Proton (O1)	0.671	0.000

Further calculations on Co^{2+}-Ti^{4+} proximity

To fully model the range of possibilities for Co^{2+} and Ti^{4+} placement a further set of calculations investigated the possibility of having Co^{2+} and Ti^{4+} in the same unit cell but not adjacent to one another, as a Co^{2+}-O-P-O-Al-O-Ti^{4+} "next-neighbour" system were modelled using eq. 1. It was found that this was more energetically favourable than the isolated system, though less favourable than the adjacent bimetallic system:

Table S12: Calculated energy differences for bimetallic $Co^{2+}Ti^{4+}$AlPO-5 unit cells

System	**E_{clu}/kJ mol^{-1}**
Isolated	0.0
Adjacent	-66.6
Next-neighbour	-22.8

The possibility of having Co^{2+} and Ti^{4+} separated further was not examined as due to the vast distances between them this would simply count as being two isolated sites.

Table S13: Proton positions and corresponding energy values in bimetallic $Co^{2+}Ti^{4+}$AlPO-5, containing a Co-O-Ti bridge.

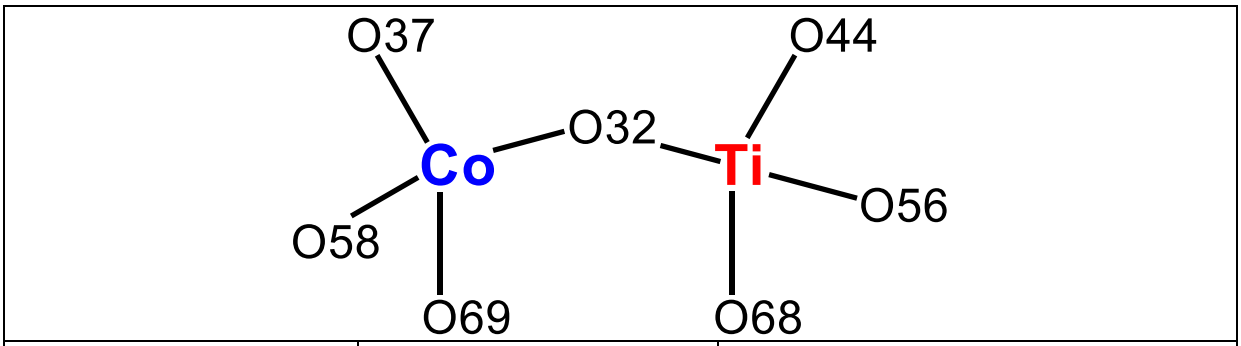

Oxygen attached to H1	Oxygen attached to H2	Relative energy difference/kJ mol^{-1}
32	58	55.2
68	58	84.7
44	58	104.9
56	58	103.7
32	32	89.1
68	32	1.2 (Close in energy)
44	**32**	**0.0 (MINIMUM VALUE)**
56	32	46.6
32	37	85.7
68	37	123.3
44	37	552.3
56	37	135.7
32	69	47.7
68	69	88.9
44	69	99.9
56	69	112.4

Table S14: Proton positions and corresponding energy values in bimetallic $Co^{2+}Ti^{4+}$AlPO-5, without a Co-O-Ti bridge.

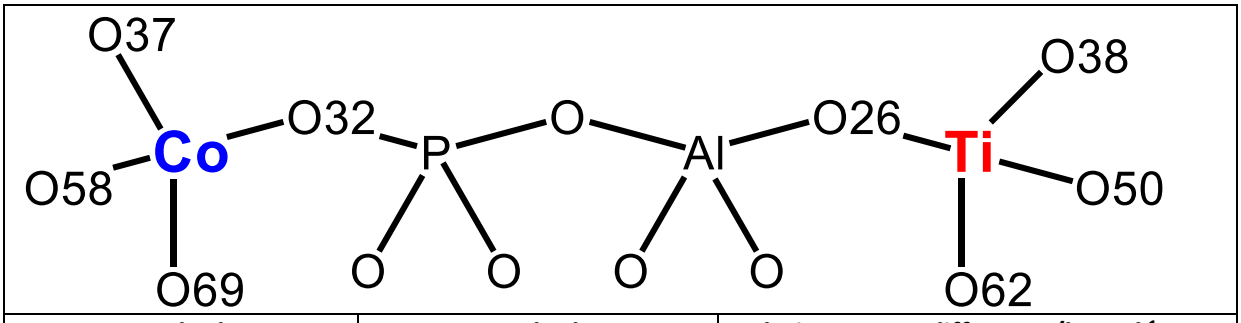

Oxygen attached to H1	Oxygen attached to H2	Relative energy difference/kJ mol^{-1}
38	58	20.0
26	58	19.6

62	58	31.0
50	**58**	**0.0 (MINIMUM VALUE)**
50	32	42.2
62	32	51.3
26	32	67.9
38	32	65.8
38	37	57.2
26	37	49.3
62	37	28.7
50	37	44.8
38	69	41.5
26	69	39.9
62	69	50.2
20	69	19.2

Further computation data on bimetallic $Co^{2+}Ti^{4+}$AlPO-5, containing a Co-O-Ti bridge

Table S15: Bond lengths in bimetallic $Co^{2+}Ti^{4+}$AlPO-5, containing a Co-O-Ti bridge.

Atom 1	**Atom 2**	**Bond length/Å**
Co1	O1 (H1)	1.973
Co1	O2	1.909
Co1	O3	1.782
Co1	O4	2.005
Ti1	O1 (H1)	1.961
Ti1	O5 (H2)	1.983
Ti1	O6	1.731
Ti1	O7	1.719
O2	P1	1.514
O3	P2	1.519
O4	P3	1.540
O5 (H2)	Al1 (H2)	1.801
O6	Al2	1.703
O7	Al3	1.731
Co1	Ti1	3.266
Co1	P1	3.162
Co1	P2	2.935
Co1	P3	2.927
Ti1	Al1 (H2)	3.535
Ti1	Al2	3.210
Ti1	Al3	3.256
O1	H1	0.973
O5	H2	0.982

Co1	H1	2.488
Ti1	H1	2.624
Ti1	H2	2.494

Table S16: Calculated Mulliken populations for bimetallic $Co^{2+}Ti^{4+}$AlPO-5, containing a Co-O-Ti bridge.

Atom	**Placement**	**Electron count (α + β)**	**Electron spin (α – β)**
Co1	Central atom	25.426	2.686
Ti1	Central atom	19.952	0.005
O1 (H)	First coordination shell (Co1 & Ti1)	8.942	0.051
O2	First coordination shell (Co1)	9.078	0.061
O3	First coordination shell (Co1)	9.083	0.085
O4	First coordination shell (Co1)	9.095	0.075
O5 (H)	First coordination shell (Ti1)	8.960	0.000
O6	First coordination shell (Ti1)	9.030	0.001
O7	First coordination shell (Ti1)	9.016	0.000
P1	Second coordination shell (O2)	12.788	0.005
P2	Second coordination shell (O3)	12.809	0.006
P3	Second coordination shell (O4)	12.797	0.004
Al1	Second coordination shell (O5)	11.052	0.000
Al2	Second coordination shell (O6)	11.063	0.000
Al3	Second coordination shell (O7)	11.066	0.000
H1	Proton (O1)	0.671	0.000
H2	Proton (O5)	0.647	0.000

Further computation data on bimetallic $Co^{3+}Ti^{4+}$AlPO-5, containing a Co-O-Ti bridge

Table S17: Bond lengths in bimetallic $Co^{3+}Ti^{4+}$AlPO-5, containing a Co-O-Ti bridge.

Atom 1	**Atom 2**	**Bond length/Å**
Co1	O1	1.757
Co1	O2	1.860
Co1	O3	1.743
Co1	O4	1.931
Ti1	O1	1.928
Ti1	O5 (H1)	1.988
Ti1	O6	1.744
Ti1	O7	1.768
O2	P1	1.534
O3	P2	1.534
O4	P3	1.557
O5 (H1)	Al1 (H1)	1.805

O6	Al2	1.665
O7	Al3	1.726
Co1	Ti1	3.158
Co1	P1	3.166
Co1	P2	2.999
Co1	P3	3.085
Ti1	Al1 (H1)	3.522
Ti1	Al2	3.126
Ti1	Al3	3.234
O5	H1	0.975
Ti1	H1	2.499

Table S18: Calculated Mulliken populations for bimetallic $Co^{3+}Ti^{4+}$AlPO-5, containing a Co-O-Ti bridge.

Atom	**Placement**	**Electron count (α + β)**	**Electron spin (α – β)**
Co1	Central atom	25.165	3.008
Ti1	Central atom	19.995	0.020
O1	First coordination shell (Co1 & Ti1)	8.977	0.419
O2	First coordination shell (Co1)	9.072	0.141
O3	First coordination shell (Co1)	9.040	0.170
O4	First coordination shell (Co1)	9.079	0.168
O5 (H)	First coordination shell (Ti1)	8.952	0.002
O6	First coordination shell (Ti1)	9.040	0.006
O7	First coordination shell (Ti1)	9.046	0.011
P1	Second coordination shell (O2)	12.767	0.005
P2	Second coordination shell (O3)	12.777	0.005
P3	Second coordination shell (O4)	12.762	0.004
Al1	Second coordination shell (O5)	11.050	0.000
Al2	Second coordination shell (O6)	11.067	0.000
Al3	Second coordination shell (O7)	11.068	0.000
H1	Proton (O5)	0.661	-0.001

Further computation data on bimetallic $Co^{2+}Ti^{4+}$AlPO-5, without a Co-O-Ti bridge

Table S19: Bond lengths in bimetallic $Co^{2+}Ti^{4+}$AlPO-5, without a Co-O-Ti bridge.

Atom 1	**Atom 2**	**Bond length/Å**
Co1	O1 (H1)	2.074
Co1	O2	1.884
Co1	O3	1.903

Co1	O4	1.897
Ti1	O5 (H2)	1.969
Ti1	O6	1.750
Ti1	O7	1.767
Ti1	O8	1.767
O1 (H1)	P1 (H1)	1.619
O2	P2	1.515
O3	P3	1.515
O4	P4	1.532
O5 (H2)	Al1 (H2)	1.784
O6	Al2	1.708
O7	Al3	1.701
O8	Al4	1.671
Co1	P1 (H1)	3.295
Co1	P2	3.267
Co1	P3	3.137
Co1	P4	3.207
Ti1	Al1 (H2)	3.465
Ti1	Al2	3.315
Ti1	Al3	3.253
Ti1	Al4	3.216
O1	H1	0.994
O5	H2	0.986
Co1	H1	2.675
Ti1	H2	2.549

Table S20: Calculated Mulliken populations for bimetallic $Co^{2+}Ti^{4+}$AlPO-5, without a Co-O-Ti bridge.

Atom	**Placement**	**Electron count (α + β)**	**Electron spin (α – β)**
Co1	Central atom	25.388	2.722
Ti1	Central atom	19.975	0.006
O1 (H)	First coordination shell (Co1)	8.903	0.026
O2	First coordination shell (Co1)	9.082	0.078
O3	First coordination shell (Co1)	9.071	0.069
O4	First coordination shell (Co1)	9.078	0.066
O5 (H)	First coordination shell (Ti1)	8.975	0.000
O6	First coordination shell (Ti1)	9.059	0.000
O7	First coordination shell (Ti1)	9.067	0.000
O8	First coordination shell (Ti1)	9.071	0.000
P1	Second coordination shell (O1)	12.755	0.002
P2	Second coordination shell (O2)	12.786	0.006
P3	Second coordination shell (O3)	12.793	0.006

P4	Second coordination shell (O4)	12.798	0.007
Al1	Second coordination shell (O5)	11.062	0.000
Al2	Second coordination shell (O6)	11.070	0.000
Al3	Second coordination shell (O7)	11.062	0.000
Al4	Second coordination shell (O8)	11.067	0.000
H1	Proton (O1)	0.634	0.000
H2	Proton (O5)	0.654	0.000

Further computation data on bimetallic $Co^{3+}Ti^{4+}$AlPO-5, without a Co-O-Ti bridge

Table S21: Bond lengths in bimetallic $Co^{3+}Ti^{4+}$AlPO-5, without a Co-O-Ti bridge.

Atom 1	**Atom 2**	**Bond length/Å**
Co1	O1	1.847
Co1	O2	1.838
Co1	O3	1.752
Co1	O4	1.859
Ti1	O5 (H1)	1.966
Ti1	O6	1.754
Ti1	O7	1.767
Ti1	O8	1.759
O1	P1	1.544
O2	P2	1.541
O3	P3	1.555
O4	P4	1.545
O5 (H1)	Al1 (H1)	1.778
O6	Al2	1.703
O7	Al3	1.702
O8	Al4	1.700
Co1	P1	3.223
Co1	P2	3.184
Co1	P3	3.109
Co1	P4	3.131
Ti1	Al1 (H1)	3.427
Ti1	Al2	3.293
Ti1	Al3	3.213
Ti1	Al4	3.213
O5	H1	0.983
Ti1	H1	2.561

Table S22: Calculated Mulliken populations for bimetallic $Co^{3+}Ti^{4+}$AlPO-5, without a Co-O-Ti bridge.

Atom	**Placement**	**Electron count**	**Electron spin**

		(α + β)	(α – β)
Co1	Central atom	25.106	3.071
Ti1	Central atom	19.984	0.000
O1	First coordination shell (Co1)	9.040	0.240
O2	First coordination shell (Co1)	9.045	0.213
O3	First coordination shell (Co1)	9.038	0.203
O4	First coordination shell (Co1)	9.051	0.177
O5 (H)	First coordination shell (Ti1)	8.971	0.000
O6	First coordination shell (Ti1)	9.066	0.000
O7	First coordination shell (Ti1)	9.070	0.000
O8	First coordination shell (Ti1)	9.068	0.000
P1	Second coordination shell (O1)	12.756	0.002
P2	Second coordination shell (O2)	12.764	0.004
P3	Second coordination shell (O3)	12.774	0.002
P4	Second coordination shell (O4)	12.763	0.004
Al1	Second coordination shell (O5)	11.059	0.000
Al2	Second coordination shell (O6)	11.068	0.000
Al3	Second coordination shell (O7)	11.071	0.000
Al4	Second coordination shell (O8)	11.068	0.000
H1	Proton (O5)	0.655	0.000

References

1) A. J. Paterson, M. E. Potter, E. Gianotti and R. Raja, *Chem. Commun.*, 2011, **47**, 517-519.
2) S. R. Bare, G. E. Mickelson, A. Z. Modica Ringwelski, and N. Yang, *Rev. Sci. Instrum.,* 2006, **77**, 023105/1-023105/6.